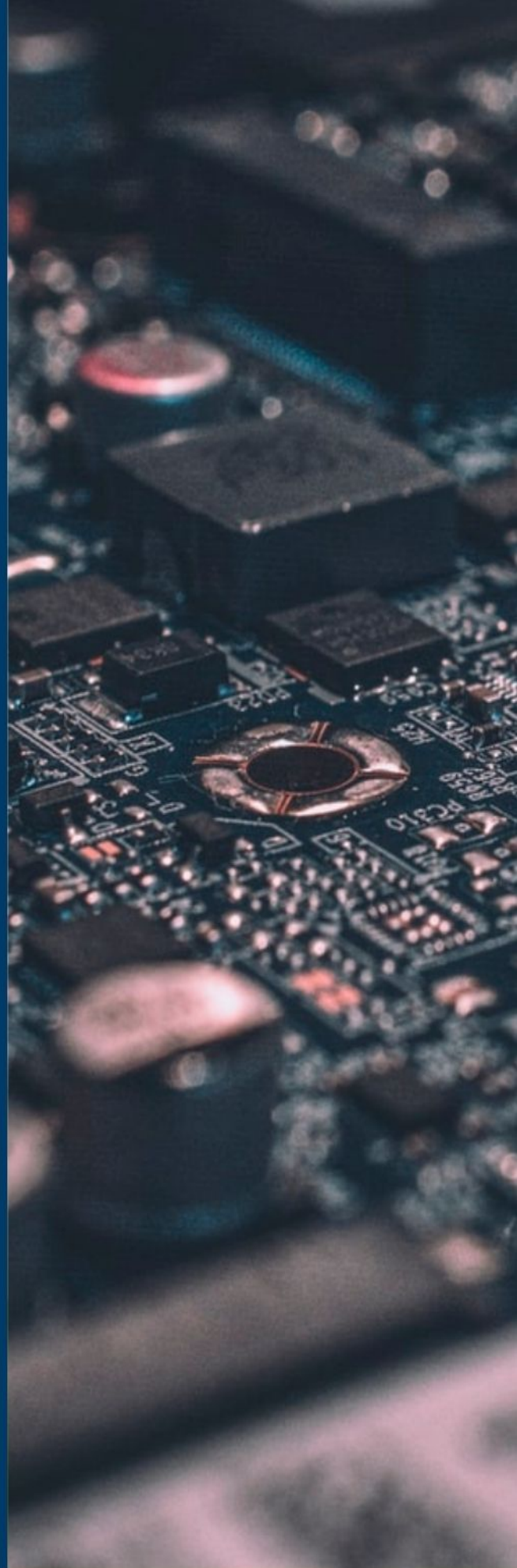# *Electronics Letters*

Special issue Call for Papers

Be Seen. Be Cited.
Submit your work to a new IET special issue

Connect with researchers and experts in your field and share knowledge.

Be part of the latest research trends, faster.

Read more

IET The Institution of Engineering and Technology

Enhancing photodetection efficiency of CMOS SiPMs using virtual guard rings in a standard 0.35 μm process

Jonathan Preitnacher,[1,✉] 🆔 Sergei Ageev,[2] and Walter Hansch[1]

[1]Institute of Physics, Bundeswehr University, Munich, Germany
[2]Research Nuclear University "MEPhI", Moscow, Russian Federation

✉ E-mail: jonathan.preitnacher@unibw.de

Fig. 1 *Cross-sectional view of the PGC (a) and VGC (b) SiPMs, illustrating their internal structure and design.*

Fig. 2 *In this figure, we can see two IV-curve graphs, one for PGC (black) and the other for VGC (red) SiPM. The first graph (a) shows the IV-curve measurements of both SiPMs taken in complete darkness. The second graph (b) illustrates the IV-curve measurements of both SiPMs when exposed to light.*

In this letter, a design of virtual guarded SiPMs fabricated in a standard 0.35μm standard complementary metal oxide semiconductor (CMOS) process is introduced. The performance of these virtual guarded cells (VGC) is compared to that of conventional cells with real guard rings, referred to as physical guarded cells (PGC). Specifically, the photon detection efficiency (PDE) of both types of SiPMs is evaluated. For this, PDE calculations are conducted at different overvoltages (OVs) and the PDE is compared depending on the wavelength before conducting measurements. The results demonstrate that the VGC SiPM outperforms the PGC SiPM, exhibiting a true PDE of $(22.5 \pm 0.5)\%$, which is significantly higher than the PDE of $(10.9 \pm 0.3)\%$ obtained for the PGC SiPM. The superior PDE of the VGC SiPM is attributed to a larger active or photosensitive area due to the virtual guard rings and a thinner n-layer in the photosensitive region.

Introduction: Silicon photomultipliers (SiPMs) consist of arrays of single photon avalanche diodes (SPADs) and are widely used in various fields, such as medical imaging [1] and high-energy physics [2]. Researchers integrate SiPMs into standard complementary metal oxide semiconductor (CMOS) processes to facilitate the integration of sensing elements and readout circuits on a single chip, thereby enhancing the performance and functionality of SiPMs. However, one of the key characteristics of these detectors are their photon detection efficiency (PDE), which is defined as the ratio of the number of detected photons to the number of incident photons. The PDE of SiPMs is given by the product of four factors [3]:

$$PDE = \epsilon \cdot IQE \cdot P_{trig} \cdot OT. \quad (1)$$

The geometrical efficiency (ϵ) refers to the proportion of the active area that is photosensitive. The internal quantum efficiency (IQE) of SiPMs refers to the probability of generating a free photoelectron in the photosensitive area of the SiPM from an incident photon. The breakdown trigger probability (P_{trig}) describes the process of multiplying the generated photoelectron through an avalanche breakdown. Additionally, the Optical Window Transparency and Reflection (OT) factor evaluates the proportion of incoming photons capable of effectively traversing the optical window without being reflected by the SiPM surface. Various techniques have been proposed to improve the PDE of SiPMs and SPADs in standard CMOS processes. One such approach involves manipulating the depth of the multiplication region to increase the PDE [4]. Other researchers try to reduce the thickness of the dead layer at the junction interface to increase the breakdown trigger probability [5]. Other techniques try to optimize ϵ and the geometry of the APD cells, for example, by replacing physical guarding with virtual guard rings for individual SPADs [6]. The technique of virtual guard rings is employed to enhance the active region of each SPAD and mitigate the effects of edge breakdown [6, 7]. Rather than employing physical guard rings, virtual guard rings are created through the overlapping of a thin, lightly doped n-region with a heavily doped n+ region, which is connected to a metal contact that serves as the cathode. The adoption of a lightly doped n+ region in combination with a slightly diminished p-well width results in a decreased electric field at the edges to prevent edge breakdown [8]. While the implementation of virtual guard rings in custom processes has gained widespread acceptance [9], their successful realization in standard CMOS technology remains a challenging task. In this study, we undertake a detailed analysis of the design of two SiPMs consisting of 254 microcells fabricated using a 0.35μm process technology. One of the
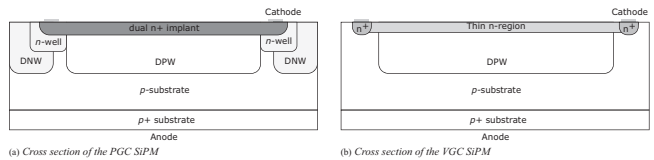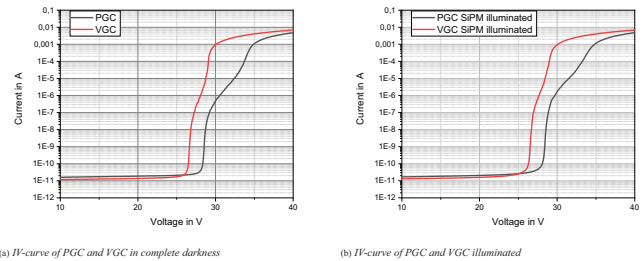
SiPMs incorporates physical guarded cells (PGC), while the other employs a approach using virtual guarded cells (VGC) without real guard rings. The SiPMs were fabricated utilizing the X-FAB foundry's standard 0.35μm CMOS technology, specifically the XH035 node.

Device structure: The cross-sectional view of both kinds of SPADs is depicted in Figures 1a and 1b. Each SPAD of both detectors had a microcell pitch of 54μm. The PGC SPAD is fabricated with a pn-junction consisting of a deep p-well (DPW) and a highly doped dual n+ implant. In order to mitigate edge breakdown effects, a conventional guard ring comprising an n-well and a deep n-well (DNW) was implemented [9]. The introduction of the DNW was selected to ensure the prevention of edge penetrations. Nevertheless, this additional n-region does not adversely affect the photosensitive area. The contact was positioned on the edges of the dual n+ implant, while the anode was formed by a p+ substrate located beneath the p substrate on the backside of the SPAD. The design of guardrings in standard CMOS processes is limited in dimensions by the constraints imposed by the fabrication facility and design rules. The VGC technology utilizes an approach in a 0.35μm CMOS to guard against corner junction breakdown without the use of physical guard rings. Instead, the VGC incorporates a thinner, less heavily doped n-type layer that overlaps with an n+ layer connected to the cathode. Based on the breakdown voltages, we suspect that the tails of the dopant profile are smoother for n+. The VGC eliminates the need for physical guard rings, which enables an 44% expanded light sensitive region between the thin n-region and the DPW, thereby enhancing the PDE. However, there was a potential risk of complete depletion of the thin n-type region due to the lower doping concentration and thinner layer. The anode is connected to the p+ layer on the rear side of the SiPM, and both the VGC and PGC SPADs were passively quenched by a polysilicon resistors with a value of $R_q = 430$kΩ. We did not employ any specific optical window processing options, which may result in a significant reduction in light intensity (up to approximately 10%) even prior to photon penetration into the semiconductor photosensitive area [10].

Standard characterization of CMOS SiPMs: For standard characterization, the current-voltage (IV) curves were obtained in both the presence and absence of a small amount of light, as depicted in Figure 2. It is noteworthy that a relatively gradual breakdown can be observed on the IV curves, which is likely attributed to the specific geometry and size of the CMOS SiPMs being investigated. The PGC and VGC SiPM exhibit breakdown voltages of 28.2 V and 26.2 V, respectively, and a punch-through voltage (which defines the second breakdown) of 35 V for the PGC and 29.5 V for the VGC with a variation of 0.1 V. The operational range for both SiPMs is up to 4 V overvoltage (OV) for the PGC and up

Table 1. Standard characterization parameters for the PGC and the VGC SiPM designs at a OV of 2V.

	PGC	VGC
Breakdown voltage:	(28.2 ± 0.1) V	(26.2 ± 0.1)V
XT:	$(2.5 \pm 0.1)\%$	$(4.0 \pm 0.1)\%$
DCR:	$(28.2 \pm 0.1)\frac{Mhz}{mm^2}$	$(2.2 \pm 0.1)\frac{Mhz}{mm^2}$
CDN:	$(48 \pm 2)\%$	$(55 \pm 3)\%$
Gain:	$(1.13 \pm 0.05) \times 10^6$	$(2.13 \pm 0.12) \times 10^6$
RC-time:	(7.2 ± 0.4)ns	(16.3 ± 0.8)ns
Operating range:	1 V− 4 V	1 V − 2.5 V

to 2.5 V OV for the VGC. Further standard parameter regarding SiPM performance are presented in Table 1, with measurements conducted at an OV of 2 V. The two SiPMs demonstrate comparable performance with noticeable differences. Both SiPMs showcase high gain, with the gain of VGC being double that of PGC. This is attributed to the larger photosensitive area achieved through a larger pn-junction, resulting in higher capacitance. High dark count rates (DCRs) are observed. At an OV of 2 V, the PGC SiPM has a DCR of (2.8 ± 0.1) MHz/mm², while the VGC SiPM exhibits a slightly lower DCR of (2.2 ± 0.1) MHz/mm². VGC SiPM exhibits a higher crosstalk rate (XT) of $(4.0 \pm 0.2)\%$, attributed to the closer proximity of its cells. Both detectors show high correlated delayed noise (CDN) of approximately 50%, including delayed crosstalk and afterpulsing events. Analyzing the magnitude and simultaneous timing of pulses allows estimating the proportion of delayed crosstalk, with an estimated value of around 70% of the pulses being delayed crosstalk pulses. Furthermore, PGC SiPM exhibits a lower recovery time due to its lower diode capacitance. The error of the measurements was determined by conducting three distinct samples and recording 10,000 measurements for each sample.

PDE calculation: Our computational approach for estimating the PDE of both PGC and VGC SiPMs employs a straightforward step-by-step approximation. Initially, we establish the stepwise triggering probability function correlated with the depth at which electron-hole pairs are generated. As documented by Antognetti [11], triggering probabilities exhibit distinctions between the n+ and p regions, with both being particularly susceptible to OV effects. We have already acquired experimentally validated probabilities for these specific areas, denoted as TPH_{OV} and TPE_{OV} [11] [12]. These probabilities are synthesized by leveraging the parameter $Xhes$, which serves as the initial component of the approximating function $P_{trig}(x)$. This function captures the gradual transition from hole-induced to electron-induced avalanches. We have replaced this continuous curve with a distinct step function that transitions between two discrete values. The depth of this step, denoted as $Xhes$, corresponds to the depth of N^+ to P junction Xj with empirical coefficient in range from 1.7 to 2 by our previous knowledge. Subsequently, we integrate XED, an estimated value representing the lower boundary of the depleted region. This parameter is derived by summing the depth of the n+ to p junction (Xj) and the thickness of the depleted region ($DEPLW$), thereby precisely defining the spatial extent of the depletion zone. We must then consider the circumstance that not all electrons generated by photons absorbed below the depleted layer within the neutral area possess the opportunity to traverse into the depleted region and thereby initiate avalanches. In the absence of an applied electric field, these electrons move randomly and can ultimately follow two equally probable directions: towards the depleted area and towards the substrate. The coefficient 0.5 present in the following expression merely reflects this phenomenon. Moreover, these 'tail' electrons necessitate a prolonged transit time to traverse the intervening region and access the multiplication area, consequently leading to compromised temporal resolution. In the following stages, a convolution of two essential functions is performed, the functional relationship that signifies light intensity I concerning depth as shown in formula 2:
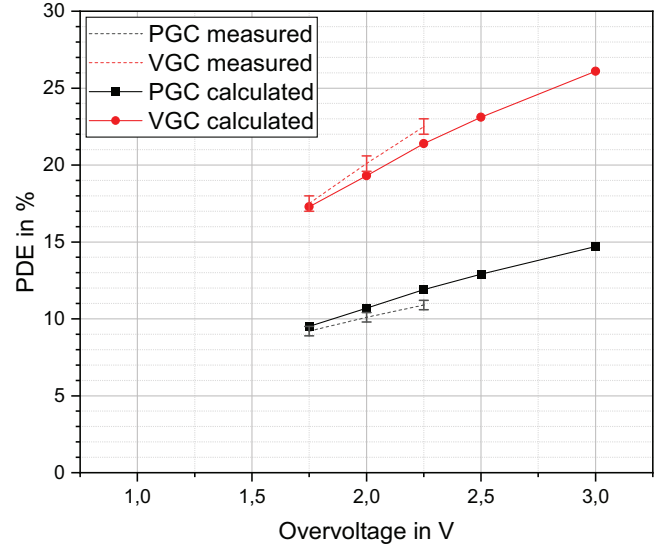
$$I = \exp\left(\frac{-x}{A_\lambda}\right), \qquad (2)$$

Fig. 3 *Calculated and measured PDE for both PGC and VGC SiPMs at varying OVs. For the calculation, we used a wavelength of λ = 460 nm, and for the measurements, λ = 463 nm.*

and the previously outlined stepwise approximation of triggering probability P_{trig} with respect to depth. The mathematical expression that governs the calculation of PDE is thus formulated as follows:

$$
\begin{aligned}
PDE_{\lambda,OV} = \bigg(& (1 - e^{-\frac{Xhes}{A_\lambda}}) \cdot TPH_{OV} \\
& + (e^{-\frac{Xhes}{A_\lambda}} - e^{-\frac{XED}{A_\lambda}}) \cdot TPE_{OV} \\
& + e^{-\frac{XED}{A_\lambda}} \cdot TPE_{OV} \cdot 0.5 \bigg) \cdot \epsilon \cdot OT
\end{aligned}
\qquad (3)
$$

In the provided expression, the symbol λ represents the wavelength of the incident light. The coefficient A_λ denotes the wavelength-specific absorption coefficient, characterizing the light absorption capability of the material under consideration. We conducted PDE calculations across various OVs encompassing 1.75 V, 2 V, 2.25 V, 2.5 V, and 3 V, while maintaining a constant wavelength λ of 460 nm. As for the junction depth Xj, we determined values of 0.2 µm for the PGC and 0.1 µm for the VGC based on X-FAB data. Moreover, we approximated the Optical Window Transparency (OT) based on the layered composition within our fabrication procedure, resulting in an approximate value of 0.96. The outcomes of these computational analyses are illustrated in Figure 3.

The calculations demonstrate that our CMOS SiPM yields a calculated PDE of 11.9% for the PGC configuration at 2.25 V, and 21.4% for the VGC configuration at the same voltage. Furthermore, when considering an OV of 3 V for both SiPM configurations, the calculated PDE stands at 14.7% for PGC and 26.1% for VGC. Moreover, we conducted PDE calculations across a wavelength spectrum, using an OV of 2.25 V, ranging from λ = 400 nm to λ = 700 nm. The outcomes of these calculations are visually depicted in Figure 4. Notably, the PGC SiPM achieves its highest PDE value at λ = 500 nm, while the VGC SiPM reaches its PDE peak at λ = 480 nm.

Photon detection efficiency measurement: The setup for our measurements was proposed and described in [[3]]. We performed measurements to determine the true PDE of our designed CMOS SiPM, with excluding XT and APP. For illumination, we used the 463 nm wavelength. The temperature was maintained at 293.15 K. The results of the PDE measurements are depicted in Figure 3. The error bars denote the standard error of the mean value, obtained from the three measurement cycles. The presented PDE data accounts for CDN effects (i.e. they are excluded). In order to obtain precise and reliable PDE values, a voltage range of 1.75 V OV to 2.25 V OV was chosen for the measurements. This range was determined by taking into account several factors, including pulse height, noise factors, especially CDN, and the operating
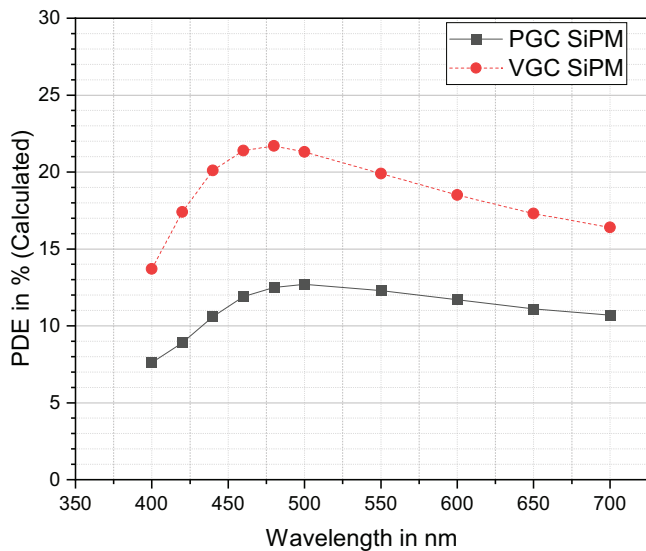
Fig. 4 *Calculated PDE for PGC and VGC SiPMs at different wavelengths with an OV of 2.25 V.*

range of the VGC SiPM. As shown in Figure 3, the PDE values of both SiPM increase proportionally with increasing OV. The PGC SiPM achieves a maximum PDE of $(10.9 \pm 0.3)\%$, while the VGC SiPM attains a PDE more than twice as high, at $(22.5 \pm 0.5)\%$, both at an OV of 2.25 V.

Discussion: Our investigation reveals a remarkable enhancement in the PDE of our VGC SiPM, surpassing the performance of our conventional PGC SiPM by a factor of 2.06 at an OV of 2.25 V and a measured wavelength of $\lambda = 463$ nm. This striking improvement in PDE can be attributed to two pivotal factors, as indicated by Equation (1). First, our approach yields a significant 44% augmentation in the photosensitive area, consequently elevating ϵ and, therefore, the PDE. Second, the VGC SiPM's thinner and less heavily doped layer facilitates a broader absorption region, amplifying P_{trig}. These explanations find support in our calculations, which, based on these parameters, forecast a similar enhancement, as demonstrated in Figure 3. Disparities evident in the rate of change of PDE values per OV can be ascribed to the simplifications introduced in our calculations to accommodate the step-like behavior. Our calculations reveal that the PGC SiPM attains its peak PDE at $\lambda = 500$ nm, while the VGC SiPM achieves its maximum at $\lambda = 480$ nm. Incorporating this distinction into our analysis could potentially marginally diminish the amplification factor. Furthermore, our findings also disclose comparable standard characterization parameters for both SiPMs. Nevertheless, it's important to highlight that the VGC SiPM demonstrates a limited operational range. To expand this operational range and potentially attain markedly higher PDE values, additional research becomes imperative. The computations presented in Figure 3 delineate the prospective enhancement of PDE as a function of OV, projecting an achievable PDE of 26.1% for VGC and 14.7% at an OV of 3 V for PGC. Comparable findings have been corroborated in previous investigations, offering compelling evidence of heightened PDE with increased OV [13, 14]. Furthermore, the integration of an optical window equipped with an anti-reflective coating holds the potential to further enhance the PDE [10]. This cumulative insight underscores the latent capacity for a substantial augmentation of the PDE through further refinement in cell design.

Conclusion: In this letter, a virtual guarded SiPM has been presented in standard CMOS 0.35μm, and its performance has been compared to a conservatively guarded SiPM in the same technology node. The results of our approach show a remarkable increase in the PDE from $(10.9 \pm 0.3)\%$ to $(22.5 \pm 0.5)\%$ at an OV of 2.25 V and a wavelength of 463 nm, which is a factor greater than 2.

Author contributions: Jonathan Preitnacher: Conceptualization, data curation, investigation, visualization, writing - original draft, writing - review and editing. Sergei Ageev: Formal analysis, methodology, writing - review and editing. Walter Hansch: Project administration, supervision.

References

1 Herrnsdorf, L., Caccia, M., Mattsson, S.: Silicon photomultipliers for medical imaging and dosimetry—an overview. *Radiat. Prot. Dosim.* **169**(1-4), 430–435 (2016)

2 Garutti, E., et al.: Silicon photomultiplier characterization and radiation damage investigation for high energy particle physics applications. *J. Instrum.* **9**, C03021 (2014). https://doi.org/10.1088/1748-0221/9/03/C03021

3 Schmailzl, W., et al.: Characterization of the photo-detection efficiency temperature dependence of silicon photomultipliers from $-30°$C to $70°$C. *J. Instrum.* **17**(12), P12009 (2022). https://doi.org/10.1088/1748-0221/17/12/P12009

4 Dalla-Betta, G.F., et al.: Avalanche photodiodes in submicron CMOS technologies for high-sensitivity imaging. In: Advances in Photodiodes, pp. 225–248. Intech, London (2011). http://www.intechopen.com/books/advances-in-photodiodes/avalanche-photodiodes-in-submicron-cmos-technologies-for-high-sensitivity-imaging

5 Mazzillo, M., et al.: Quantum detection efficiency in geiger mode avalanche photodiodes. *IEEE Trans. Nucl. Sci.* **55**(6), 3620–3625 (2008)

6 Shin, D., et al.: The effect of a deep virtual guard ring on the device characteristics of silicon single photon avalanche diodes. *IEEE Trans. Electron. Devices* **66**(7), 2986–2991 (2019)

7 Bandi, F., et al.: Architecture-level optimization on digital silicon photomultipliers for medical imaging. *Sensors* **22**(1), 122 (2022)

8 Sul, W.S., et al.: Guard-ring structures for silicon photomultipliers. *IEEE Electron Device Lett.* **31**, 41–43 (2010)

9 Acerbi, F., Gundacker, S.: Understanding and simulating sipms. *Nuclear Instr. Meth. Phys. Res. Sect. A: Accelerators Spectrometers Detectors Associated Equip.* **926**, 16–35 (2019)

10 D'Ascenzo, N., et al.: A novel high photon detection efficiency silicon photomultiplier with shallow junction in 0.35 μm CMOS. *IEEE Electron Device Lett.* **40**(9), 1471–1474 (2019)

11 Antognetti, P., Oldham, W.G.: The role of ionization coefficient in the operation of avalanche diodes above breakdown. *J. Electron. Mater.* **4**(1), 77–90 (1975)

12 Muller, R.S., Kamins, T.I.: *Device Electronics for Integrated Circuits.* 3rd ed. Wiley, New York (2002)

13 Shimada, S., et al.: A back illuminated 6μm spad pixel array with high pde and timing jitter performance. In: 2021 IEEE International Electron Devices Meeting (IEDM), pp. 20.1.1–20.1.4. IEEE, Piscataway (2021)

14 Gallina, G., et al.: Characterization of sipm avalanche triggering probabilities. *IEEE Trans. Electron Devices* **66**(10), 4228–4234 (2019)